Elaboration of A Coupled Numerical Model for Predicting Magnesia Refractory Damage Behavior in High-Temperature Reactor

QIANG WANG a,b,), CHONG TAN a,b), CHANG LIU a,b), ZHIYUAN CHEN c), WEN YAN a,b),
QIANG WANG d), and GUANGQIANG LI a,b,*)
a) The State Key Laboratory of Refractories and Metallurgy, Wuhan University of Science and Technology, Wuhan, Hubei 430081, China.
b) Key Laboratory for Ferrous Metallurgy and Resources Utilization of Ministry of Education, Wuhan University of Science and Technology, Wuhan, Hubei 430081, China.
c) Separation and Conversion Technology, Flemish Institute for Technological Research (VITO), Mol 2400, Belgium.
d) Key Laboratory of Electromagnetic Processing of Materials (Ministry of Education), Northeastern University, Shenyang, Liaoning 110819, China.

ABSTRACT

A quantitative evaluation method for the magnesia refractory deterioration in the smelting process is proposed based on analysis of static and rotating finger tests to study the dissolution behavior. A transient 3D fluid-solid coupled numerical model was then developed, including the two-phase gas/slag flow pattern, temperature profile, MgO content distribution, solid refractory dissolution, and sample shape change. A kinetic degradation model was introduced to calculate the refractory overall wear rate determined by the coupled effect of the flow-induced erosion and chemical-induced corrosion. The shape change of the solid refractory sample was characterized *via* the dynamic mesh technique. A close correlation between the simulated results and the experimental data gives confidence in the fundamental validity of the developed numerical model.

---

* Corresponding author. Tel.: +86-27-68862085; Fax: +86-27-68862085.
E-mail address: liguangqiang@wust.edu.cn

The results indicate that the flow would increase the overall wear rate by one or two orders of magnitude depending on the velocity. Therefore, flow-induced erosion must be accounted for in estimating the refractory wear rate. The flow-induced erosion and chemical-induced corrosion could be quantified *via* the wall shear stress and a modified Arrhenius's law, respectively.

KEYWORDS: degradation behavior; magnesia refractory; slag-refractory reaction; numerical simulation.

NOMENCLATURE

$c_{p,g}$	specific heat of argon gas at constant pressure (J/(kg·K))
$c_{p,r}$	specific heat of refractory sample at constant pressure (J/(kg·K))
$c_{p,s}$	specific heat of molten slag at constant pressure (J/(kg·K))
d	characteristic length of refractory sample (m)
$D_{\mathrm{MgO},\,r}$	diffusion coefficient of MgO in refractory sample (m^2/s)
$D_{\mathrm{MgO},\,s}$	diffusion coefficient of MgO in molten slag (m^2/s)
Ea	activation energy of magnesia refractory (J/mol)
$\overline{E}$	internal energy of mixture liquid phase (J/m^3)
$\vec{F}_{st}$	interface tension (N)
h_r	sensible enthalpy of refractory sample (J/kg)
$k_{T,\,eff}$	effective thermal conductivity of mixture liquid phase (W/(m·K))
$k_{T,\,r}$	thermal conductivity of refractory sample (W/(m·K))
$k_{w,\,eff}$	effective coefficient used in Eq. [11]
L	penetration depth of molten slag to refractory sample (m)
$\vec{n}_r$	unit normal vector to fluid-solid interface in refractory sample
$\vec{n}_s$	unit normal vector to fluid-solid interface in molten slag
p	pressure (Pa)
R	universal gas constant (J/(mol·K))
R_w	overall wear rate (kg/s)
Sc_t	turbulent Schmidt number
T	temperature (K)

T_{ref}	reference temperature (K)
t	time (s)
V_{cell}	volume of computational cell (m^3)
$\vec{v}$	velocity of mixture liquid phase (m/s)
$\vec{v}_m$	velocity of moving mesh (m/s)
$w_{\mathrm{MgO},\, r}$	MgO mass fraction in refractory lining (%)
$w_{\mathrm{MgO},\, s}$	MgO mass fraction in molten slag (%)

GREEK SYMBOLS

α	volume fraction of molten slag
θ	contact angle between molten slag and refractory sample (°)
$\bar{\mu}$	dynamic viscosity of mixture liquid phase (Pa·s)
μ_s	dynamic viscosity of molten slag (Pa·s)
μ_t	turbulent viscosity (Pa·s)
$\bar{\rho}_\ell$	density of mixture liquid phase (kg/m^3)
ρ_g	density of argon gas (kg/m^3)
ρ_r	density of refractory sample (kg/m^3)
ρ_s	density of molten slag (kg/m^3)
σ	interface tension coefficient (N/m)
τ	wall shear stress (Pa)
τ_t	high temperature torsional strength of refractory sample (Pa)
φ	porosity of refractory sample
χ	tortuosity of refractory sample
$\bar{\phi}$	physical property of mixture liquid phase

ϕ_g	physical property of argon gas
ϕ_s	physical property of molten slag

I. INTRODUCTION

Magnesia (MgO) and magnesium oxide-containing refractory materials are widely used in various high-temperature process industries such as metal production and glass industries due to their high-temperature resistant properties.[1-3] As they can basically maintain their strength at high temperature, these refractory materials are applied to adhere structural components within the high-temperature reactors, without the risk of collapse.[4-6] However, damage to the reactor linings would occur because of flow-induced abrasion and chemical-induced corrosion, especially in the steelmaking process.[7,8] The high density molten steel carries a great amount of momentum which promotes flow-induced abrasion. In addition, molten oxides, also named molten slag, are employed in the steelmaking process, giving rise to chemical-induced corrosion.

The wear of refractory materials reduces the lining service life and harms the steel quality, because exogenous inclusions would be introduced in molten steel from the dissolution of the refractory.[9-11] Furthermore, the exogenous inclusions are often larger than endogenous inclusions of oxides and sulfides creating defects in steel products and sometimes causing the nozzle clogging.[12] Therefore, the degradation of refractory lining must be strictly monitored to maintain the refractory's strength in the steelmaking processes for product quality improvement.[13]

Due to the hostile environment in actual steelmaking processes, observing the lining running condition and measuring the lining wear rate with acceptable accuracy is problematic. With the development of numerical techniques and computational resources, the computational fluid dynamics (CFD) approach has become a powerful alternative tool for analyzing the wear behavior of the refractory lining in actual smelting processes.[14-17] It was reported that the refractory lining erosion created by the molten steel flow could be numerically studied. The complicated flow pattern and temperature map were first analyzed using the appropriate turbulent and heat transfer models. The calculated wall shear stress was employed to predicate the refractory lining erosion rate. Besides, the shape change of the refractory lining was also estimated by a fluid-solid-coupled model according to refractory properties such as the Young Modulus and Poisson's ratio.[18] Moreover, the resultant exogenous inclusion formation and evolution were studied using the Euler-Lagrange approach.[18] However, the refractory lining corrosion generated by the molten slag was investigated through high-temperature experiments and thermodynamic calculation instead of numerical simulation.[19] The laboratory static and rotating finger tests were widely employed to study the interaction between the refractory and molten slag.[20] The dissolution and microstructure change of the refractory, and the newly formed exogenous inclusion were observed using a scanning electron microscope, while the component distribution was detected using X-ray fluorescence. However, the laboratory experimental results are hard to directly relate to industrial applications because the experimental conditions differ from those in industrial production. Moreover, no quantitative description of the laboratory test results has been developed yet.[21] Several kinetic models were established with the simplified consideration of fluid flow and heat transfer.[22-24] These studies, however, focused on the variation of composition and microstructure near the slag/refractory interface but not on the overall corrosion rate of the refractory lining, which has a considerable effect on the structural design of metallurgical vessels. The general corrosion rate of the refractory lining is a time-dependent variable influenced by the refractory and slag compositions, as well as by the flow and heat transfer. Investigating the dissolution behavior of sintered MgO and commercial MgO-C and MgO-Cr_2O_3 refractories in a synthesized 50CaO-45Al_2O_3-5SiO_2 (mass%) molten slag has been carried out in a previous study.[25] The refractory sample was immersed into the molten slag with 1773 K (1500 °C) heating and bottom-blowing stirring gas. The results indicated that the dissolution rates of all the refractory samples grew as the stirring gas flow rate was increased from 25 to 75 mL/min. The rotating cylinder technique was adopted to study the flow effect on the dense magnesia specimen dissolution in the CaO-Al_2O_3 slag. The forced convection and temperature strongly affected the refractory sample dissolution rate. Moreover, the dissolution was controlled by mass transfer in the molten slag, especially the diffusivity of MgO.[26-28]

As discussed above, it is hard to find a numerical simulation of the chemical-induced corrosion on refractory which could comprehensively consider the composition, flow and temperature effects. The authors were therefore motivated to conduct static and rotating finger tests to clarify the magnesia refractory damage behavior. Based on the experimental results, a transient 3D fluid-solid coupled numerical model was developed to describe the evolution of the flow, temperature profile, and compositional concentration distribution. The shape change of the solid refractory sample over time was also clarified. Variations of the component concentration and refractory sample shape and mass loss were carefully compared between the experiment and simulation for model validation. The proposed numerical model is believed to be applicable to study various refractory lining damage scenarios in industrial-scale metallurgical units.

II. EXPERIMENTS

A. *Refractory Sample and Slag Preparation*

The refractory sample was prepared in the laboratory using magnesite powder (Liaoning Magnesite Materials Co., Ltd., China), which was a powder mixture from five different particle size groups (0-0.088 mm, 0.088-1 mm, 1-3 mm, 3-5 mm, and 5-8 mm). Besides, reagent grade MgO powder, dispersing agent, and water were added to the refractory sample. The exact proportion of each raw material is displayed in **Table I**. The initial MgO concentration of the refractory was around 97%, because the refractory castable also contained tiny amount of impurities such as calcium oxide and silicon oxide. These raw materials were first fully vibratory mixed and poured into a 25 × 25 × 125 mm steel mold. The castable was then cured at 293 K (20 °C) for 24 h and another 24 h at the same temperature after demolding. To remove moisture, the sample was dried at 383 K (110 °C) for 24 h and sintered at 1823 K (1550 °C) for 3 h.[26]

Table I. Preparation formula of the refractory sample (wt. %)

Magnesia particle					MgO powder (<0.088mm)	Dispersing agent	Extra water
8-5mm	5-3mm	3-1mm	1-0mm	<0.088mm			
10%	27%	18%	17%	23%	5%	0.2%	4%

A typical tundish covering slag was prepared using analytical reagents including CaO, Al_2O_3, SiO_2, and MgO (Sinopharm Chemical Reagent Co., Ltd., China), as shown in **Table II**. After mechanical mixing, the slag powder was kept for 12 h at 1273 K (1000 °C) in a graphite crucible and then pre-melted at 1773 K (1500 °C) for 30 min using an electrical resistance furnace.[29]

Table II. Initial composition of molten slag (wt.%)

CaO	Al_2O_3	SiO_2	MgO
45.00	40.00	5.00	10.00

B. *Experimental Setup and Procedure*

Fig. 1 shows a schematic of the experimental device. The sintered magnesia castable was machined into a 25 × 25 × 62 mm sample. The sample was then dried at 383 K (110 °C) for 24 h to remove moisture. To keep the sample stable in the rotating process, a molybdenum bar, which could provide enough rigidity at high temperature, was used to connect the cuboid-shaped refractory sample and the stirring motor. A measured quantity of 100 g pre-melted slag was first held at 1273 K (1000 °C) in a muffle furnace to remove moisture and placed inside a graphite crucible (inner diameter of 60 mm and internal height of 90 mm). Once the required temperature (1833 K (1560 °C)) was reached, the crucible holding the slag was placed in the constant temperature zone in the tube. The refractory sample was placed within the molten slag and remained stationary or rotated at a constant speed. To prevent oxidation, a constant flow of high-purity argon gas at a rate of 0.3 L/min was maintained during the entire experiment. After the required reaction time, the sample was raised 5 cm above the crucible and rotated at a higher speed for 5 min to remove the molten slag adhering to the sample surface. The sample was finally taken out and cooled on a copper plate.[30-32]

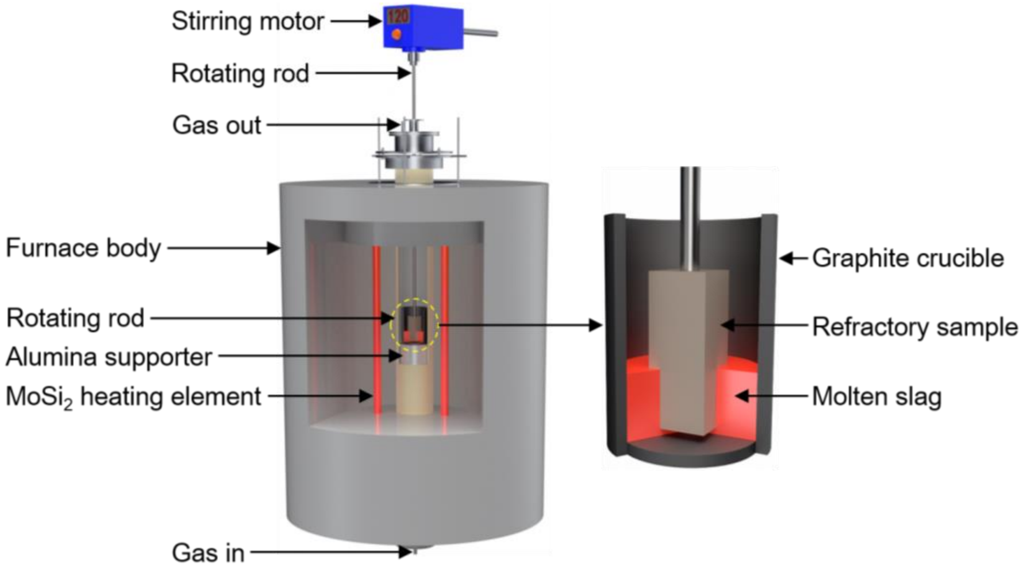

Fig. 1 – Experimental setup.

III. NUMERICAL MODEL

A. *Model Assumptions*

(a) The computational domain included both the fluid and solid. The fluid part involved the argon gas and molten slag, while the solid part only comprised the refractory sample. The graphite crucible was ignored.

(b) The argon gas and molten slag were treated as an incompressible Newtonian fluid.

(c) The density of the argon gas was treated as temperature-dependent, while all other properties were assumed to be constant.

(d) Chemical compositions other than MgO were neglected as MgO is the crucial component of the magnesia refractory and significantly influences slag corrosion.[33]

(e) The slag corrosion and the matrix dissolution that occurred inside the porous refractory after the slag infiltration were neglected.[34]

(f) The delaminated refractory from the sample was assumed to dissolve in the molten slag in the liquid state, because the fluid-solid coupled algorithm and dynamic mesh method were adopted to track the shape change of the refractory sample. The reduced solid region was assumed to be filled with the same mass molten slag for avoiding mass non-conservation during the numerical solution. The volume of the molten slag thus could be determined according to its density. Noteworthy is that this assumption is quite different from the actual situation. The delaminated refractory fragments cannot be totally melted in the molten slag when the MgO content in the molten slag gradually approaches its saturation content in the experiment. Part of the delaminated refractory fragments would dissolve in the molten slag in the solid form, generating the exogenous inclusion. In the numerical simulation, however, it is not easy to represent these phenomena, because this involves the addition of the mass source term of the solid phase and the movement of the solid refractory fragment.

B. *VOF Method*

The volume of fluid (VOF) methodology was utilized to trace the motion of the interface between the gas and molten slag.[35] It uses a scalar α representing the volume fraction of molten slag, which is between 0 and 1. The physical properties of the mixture phase, such as the density, viscosity, and thermal conductivity, are related to the volume fraction of each phase as follows:

$$\bar{\phi} = \phi_s \alpha + \phi_g \left(1 - \alpha\right) \quad [1]$$

A single set of continuity, momentum, and energy equations was established and solved in the whole fluid part of the computational domain. Moreover, the scalar α was simultaneously updated at each time step. The gas and molten slag shared the calculated velocity field and temperature distribution. Besides, the interfacial tension between the gas and molten slag was assessed using the continuum surface force model with a constant interfacial tension coefficient.[36] The wall adhesion model was used to determine the contact angle between the molten slag and the refractory.[37]

C. *Fluid Flow and Heat Transfer*

The continuity and time-averaged Navier-Stokes equations were invoked to depict the turbulent flow:[15]

$$\frac{\partial \bar{\rho}_\ell}{\partial t} + \nabla \cdot \left(\bar{\rho}_\ell \vec{v}\right) = 0 \quad [2]$$

$$\frac{\partial \left(\bar{\rho}_\ell \vec{v}\right)}{\partial t} + \nabla \cdot \left(\bar{\rho}_\ell \vec{v}\vec{v}\right) = -\nabla p + \nabla \cdot \left[\bar{\mu}\left(\nabla \vec{v} + \nabla \vec{v}^{\mathrm{T}}\right)\right] + \vec{F}_{st} \quad [3]$$

The dynamic mesh model, which could capture the shape changing of the computational domain with time, was adopted to describe the shape change of the solid region and the adjacent fluid region. The above two conservation equations on the control volume with a moving boundary can be written as in:[38-40]

$$\frac{\partial \bar{\rho}_\ell}{\partial t} + \nabla \cdot \left[\bar{\rho}_\ell \left(\vec{v} - \vec{v}_m\right)\right] = \frac{R_w}{V_{cell}} \quad [4]$$

$$\frac{\partial \left(\bar{\rho}_\ell \vec{v}\right)}{\partial t} + \nabla \cdot \left[\bar{\rho}_\ell \vec{v}\left(\vec{v} - \vec{v}_m\right)\right] = -\nabla p + \nabla \cdot \left[\bar{\mu}\left(\nabla \vec{v} + \nabla \vec{v}^{\mathrm{T}}\right)\right] + \vec{F}_{st} \quad [5]$$

where $\vec{v}_m$ is the velocity of the moving mesh. The right-hand side of Eq. [4] implies the dissolution of the solid refractory sample into the molten oxides giving rise to the mass increase of the molten slag in unit volume.

Since the damage of the refractory sample created by the turbulent flow is mainly determined by the wall shear stress, the shear-stress transport (SST) *k*-*ω* turbulence model was adopted for a better description. The SST *k*-*ω* turbulence model consists of the original Wilcox *k*-*ω* model and the standard *k*-*ε* model by a blending function, where the former applies to the flow in the wall vicinity. At the same time, the latter is more suitable for the flow within the fluid bulk. The eddy viscosity formulation was modified to account for the transport effects of the principle turbulent shear stress, yielding a highly accurate prediction of the turbulent shear stress transport. Besides, the refractory sample would get shorter with the dissolution, resulting in a weaker stirring and inactive fluid flow.

The following energy conservation equation was solved to figure out the temperature distribution and was applied to both the fluid and solid regions:[41]

In the fluid region: $$\frac{\partial\left(\bar{\rho}_{\ell}\bar{E}\right)}{\partial t}+\nabla\cdot\left(\bar{\rho}_{\ell}\bar{E}\vec{v}\right)=\nabla\cdot\left(k_{T,eff}\nabla T\right) \qquad [6]$$

where $k_{T,eff}$ is the effective thermal conductivity. It is calculated as the sum of the natural thermal conductivity and turbulent thermal conductivity defined *via* the used turbulence model. $\bar{E}$ is the internal energy of the mixture liquid phase defined *via* the two fluids' specific heats and temperatures:

$$\bar{E}=\frac{\alpha\rho_s c_{p,s}T+\left(1-\alpha\right)\rho_g c_{p,g}T}{\alpha\rho_s+\left(1-\alpha\right)\rho_g} \qquad [7]$$

In the solid region: $$\frac{\partial\left(\rho_r h_r\right)}{\partial t}=\nabla\cdot\left(k_{T,r}\nabla T\right) \qquad [8]$$

where h_r is the sensible enthalpy of the refractory sample, which is defined as follows:

$$h_r=\int_{T_{ref}}^{T}c_{p,r}dT \qquad [9]$$

For the same reason, the energy conservation equation on the control volume of the fluid region with a moving boundary can be expressed as in:[42]

$$\frac{\partial\left(\bar{\rho}_{\ell}\bar{E}\right)}{\partial t}+\nabla\cdot\left[\bar{\rho}_{\ell}\bar{E}\left(\vec{v}-\vec{v}_{m}\right)\right]=\nabla\cdot\left(k_{T,\,eff}\nabla T\right) \qquad [10]$$

The second term on the left-hand side of the above equation indicates the energy change induced by the fluid flow within the control volume, which can be neglected in the solid region. The energy conservation equation on the control volume of the fluid region with a moving boundary coincides with Eq. [8].

D. *Refractory Wear Behavior*

The refractory sample wear inevitably occurs because of the flow-induced erosion and chemical-induced corrosion. The wear rate of the refractory sample can be derived as a combined effect of physical erosion and chemical corrosion:[43-50]

$$R_{w}=k_{w,eff}\cdot\left(\frac{\tau}{\tau_{t}}\right)^{a}\cdot\left(\frac{L}{d}\right)^{b}\cdot\frac{\left(w_{\mathrm{MgO},\,r}\rho_{r}-w_{\mathrm{MgO},\,s}\rho_{s}\right)V_{cell}}{t}\cdot exp\left(-\frac{Ea}{RT}\right) \qquad [11]$$

$$L=\sqrt{\frac{\varphi\ \sigma\ t\cos\theta}{\mu_{s}}}\Big/\chi \qquad [12]$$

where τ is the wall shear stress at the interface between the molten slag and the refractory sample, which represents the flow effect on the dissolution behavior, and τ_t denotes the high-temperature torsional strength of the refractory sample. Besides, L indicates the penetration depth of the molten slag into the refractory sample, which is related to the refractory sample porosity and tortuosity, the molten slag surface tension and viscosity, and the contact angle between the molten slag and refractory sample, while d is the refractory sample characteristic length. Noteworthy is that the refractory porous and tortuosity would change with the slag infiltration, because the slag corrodes the matrix inside the porous refractory after infiltration. However, the slag corrosion and matrix dissolution were ignored in the developed model as mentioned above. Therefore, constant refractory porosity and tortuosity were used. To get closer to the actual situation, the penetration depth was assumed to increase over time under continuous corrosion of the refractory sample.

In the present model, the erosion and corrosion patterns were coupled rather than isolated. The magnesia refractory corrosion activation energy Ea used in Eq. [8] was measured in the laboratory test.[51]

The MgO concentration difference between the molten slag and the refractory sample was regarded as the driving force of the refractory sample dissolution behavior. As mentioned above, the delaminated refractory fragments were assumed to be entirely melted in the molten slag in the whole experiment. A general transport equation was therefore utilized to describe the convection and diffusion of MgO in the molten slag:[52,53]

In the fluid region: $$\frac{\partial\left(\bar{\rho}_\ell w_{\mathrm{MgO},s}\right)}{\partial t}+\nabla\cdot\left(\bar{\rho}_\ell w_{\mathrm{MgO},s}\vec{v}\right)=\nabla\cdot\left(\left(\bar{\rho}_\ell D_{\mathrm{MgO},s}+\frac{\mu_t}{Sc_t}\right)\nabla w_{\mathrm{MgO},s}\right) \quad [13]$$

It should be noted that this assumption diverges somewhat from the facts, since part of the delaminated refractory fragments would dissolve in the molten slag in the solid form after MgO becomes saturated in the molten slag. This assumption is not realistic but significantly simplified the simulation. The above equation on the control volume of the fluid region with a moving boundary can be modified as follows:

$$\frac{\partial\left(\bar{\rho}_\ell w_{\mathrm{MgO},s}\right)}{\partial t}+\nabla\cdot\left[\bar{\rho}_\ell w_{\mathrm{MgO},s}\left(\vec{v}-\vec{v}_m\right)\right]=\nabla\cdot\left(\left(\bar{\rho}_\ell D_{\mathrm{MgO},s}+\frac{\mu_t}{Sc_t}\right)\nabla w_{\mathrm{MgO},s}\right)+\frac{R_w w_{\mathrm{MgO},r}}{V_{cell}} \quad [14]$$

where the second term on the right-hand side of the above equation implies the MgO content in the newly formed molten slag generated by the dissolved refractory sample. Besides, the diffusion of MgO in the refractory sample can be expressed as follows:

In the solid region: $$\frac{\partial\left(\rho_r w_{\mathrm{MgO},r}\right)}{\partial t}=\nabla\cdot\left(\rho_r D_{\mathrm{MgO},r}\nabla w_{\mathrm{MgO},r}\right)-\frac{R_w w_{\mathrm{MgO},r}}{V_{cell}} \quad [15]$$

where the second term on the right-hand side of the above equation stands for the reduced MgO content in the refractory sample because of the dissolution. Since the MgO diffusion in the solid region would not be influenced by the fluid flow, the MgO transport equation on the control volume of the solid region with a moving boundary remained unchanged.

E. *Boundary Conditions*

Fig. 2 shows the computational domain with the exact dimensions. The detailed physical properties and operating conditions used in the simulation are listed in **Table III**. The refractory sample inserted into the molten slag was treated as a solid region in the simulation, while the argon gas and molten slag were considered as the fluid region. The moving wall boundary condition was applied to the wall and bottom of the refractory sample with a 120 rpm rotation speed to simulate the rotating working condition. Besides, a coupled thermal state was used for the refractory sample wall and bottom, and the corresponding shadow wall and bottom of the fluid region to satisfy the heat flux continuity. As for the inner wall and bottom of the graphite crucible, a no-slip wall boundary condition with reasonable convection heat transfer coefficient was utilized. The top surface of the argon gas part was assumed to be the pressure outlet with a low pressure and a constant temperature. Furthermore, MgO was allowed to come across the solid-fluid interface, which flux was determined by the respective diffusion coefficients:[15]

$$D_{\mathrm{MgO},\,r}\frac{\partial w_{\mathrm{MgO},\,r}}{\partial \vec{n}_r}=D_{\mathrm{MgO},\,s}\frac{\partial w_{\mathrm{MgO},\,s}}{\partial \vec{n}_s} \quad [16]$$

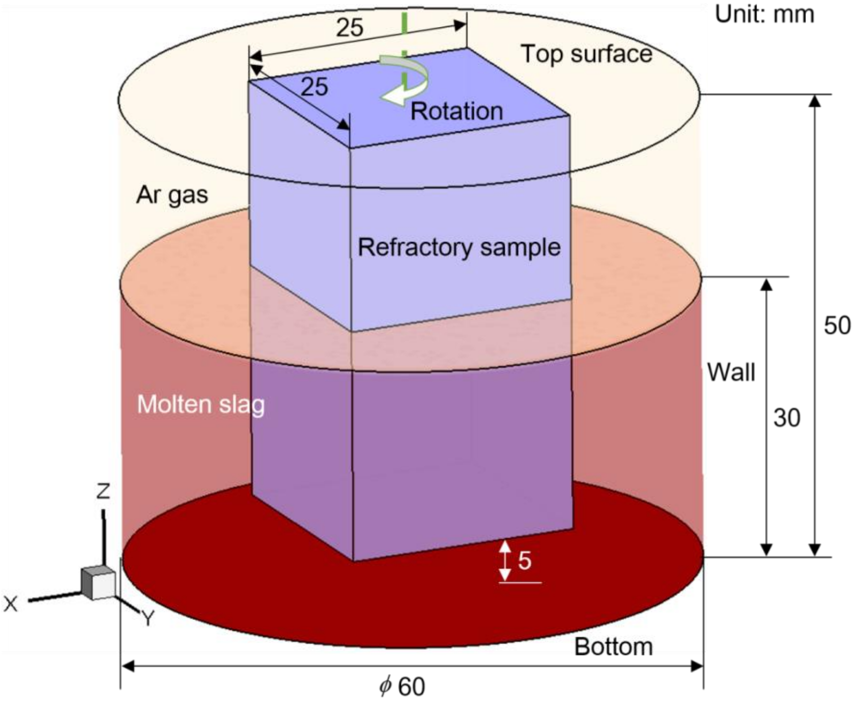

Fig. 2 – Physical model of the computational domain.

Table III. Physical Properties and Operating Conditions

Parameter	Value

Physical properties of air	
Density (kg/m^3)	3080
Apparent porosity (%)	12.7
Thermal conductivity (W/m·K)	0.025
Specific heat (J/kg·K)	1006
Physical properties of molten slag	
Density (kg/m^3)	2850
Dynamic viscosity (Pa·s)	0.25
Thermal conductivity (W/m·K)	0.15
Specific heat (J/kg·K)	825
Surface tension coefficient of molten slag (N/m)	0.54
Contact angle between molten slag and refractory (º)	46.5
Physical properties of argon gas	
Density (kg/m^3)	1.63
Dynamic viscosity (Pa·s)	4.2×10^{-5}
Thermal conductivity (W/m·K)	0.017
Specific heat (J/kg·K)	525
Thermal expansion coefficient (K^{-1})	3.4×10^{-3}
Operating conditions	
Inner diameter and height of crucible (mm)	60/80
Rotation speed (rpm)	120
Holding temperature (K)	1833

IV. SOLUTION PROCEDURE

The numerical simulation was carried out using the ANSYS Fluent 2020R1 commercial software. Two user-defined scalars were set up in the refractory sample and molten slag, respectively, representing MgO contents in the solid and fluid regions. The arithmetical expressions for the refractory wear rate were numerically run using codes developed by the authors, which were then integrated into the original software program.

The remeshing method, which is appropriate for the conditions where the boundary displacement is large compared to the size of the local cells, was utilized to assess the shape changing of the refractory sample.[54] The corresponding wear rate determined the total displacement of the control volume, and the wall shear stress defined its direction along the *X*-, *Y*-, and *Z*-axes. The update of the volume mesh was processed automatically by the ANSYS Fluent software at each time step according to the new positions of the nodes of the refractory sample wall and bottom, as well as the corresponding shadow wall and bottom of the fluid region.[55]

The momentum, turbulent kinetic energy, specific dissipation rate, energy, and user-defined scalar equations were discretized using a second-order upwind scheme for higher accuracy. The well-known PISO (pressure implicit with the splitting of operator) scheme was employed for the pressure-velocity coupling. In addition, the modified high-resolution interface capturing method was adopted as a discretization scheme for the volume fraction analysis. The convergence criteria for the continuity, momentum, turbulent kinetic energy, specific dissipation rate, user-defined scalar, and volume fraction equations were set at 10^{-6}, while that for the energy equation was 10^{-8}.

The grid independence analysis was thoroughly conducted using three families of unstructured meshes, with mean sizes of 0.2, 0.4, and 0.8 mm. In the three meshes, the value of $y+$ within the grids adjacent to the crucible wall and bottom was approximately equal to unity. After a typical simulation, the MgO contents at three monitoring points for the three types of grids were carefully compared. The average ensemble deviation of the MgO content data of the three monitoring points was about 2.55 pct for the first and second meshes, and about 5.13 pct between the second and third meshes. The complete scenario calculations for the first, second, and third meshes took about 660, 480, and 390 CPU hours using 120 cores at a basic frequency of 2.40 GHz. Considering the high computation cost, the second mesh (0.4 mm) was used in the further numerical simulations. The time step of 0.001 s was adopted for the second mesh.

V. RESULTS AND DISCUSSION

A. *Morphology Evolution of Refractory Sample in Static Testing*

Fig. 3 shows the distributions of the temperature and gas/slag two-phase in the static testing after 25 min. Due to the limited space, the temperature distribution in the crucible is very uniform, ranging from 1830 K to 1833 K. It is clear that the argon gas located at the outer ring of the upper part of the crucible is colder. Besides, the wetting phenomenon could be observed because of the application of the wall adhesion model. The contact angle used in the simulation is around 46.5 degrees according to the performed measurements.[56]

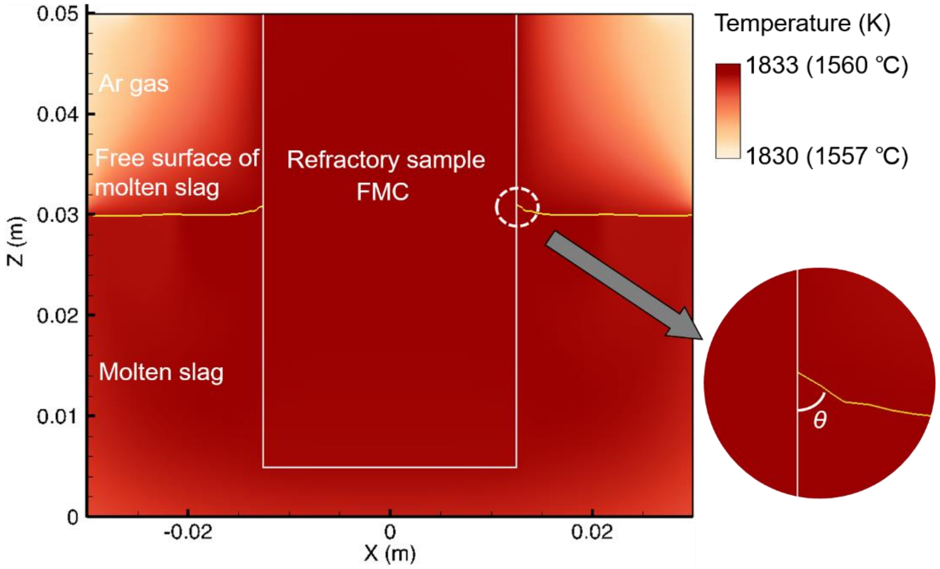

Fig. 3 – Distributions of the temperature and the gas-slag two phases in the static experiment at 25 min.

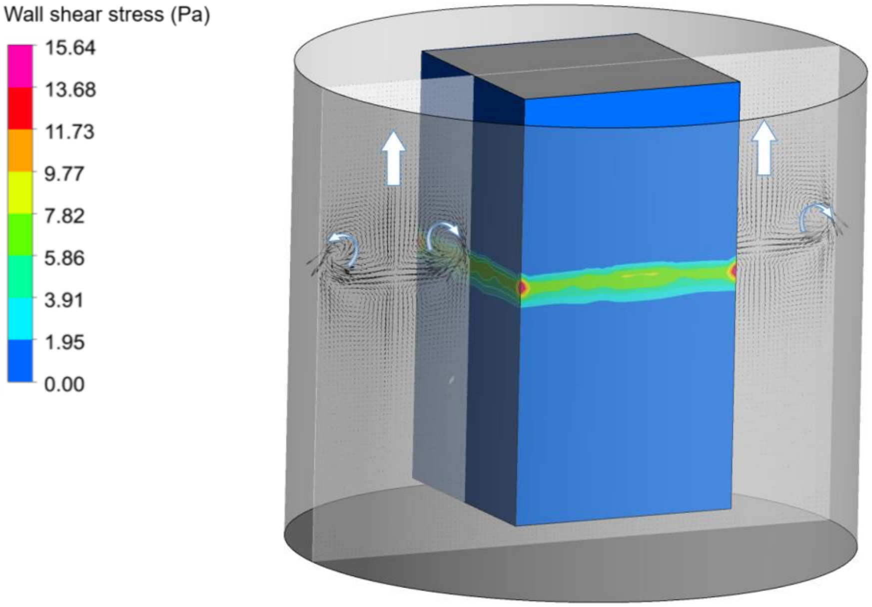

Fig. 4 – Wall shear stress distribution along the refractory sample wall and bottom in the static experiment at 25 min.

Fig. 4 displays the wall shear stress distribution along the refractory sample wall and bottom. The argon gas flows upward under the thermal buoyancy effect causing a fluctuation of the gas/slag interface working with the interfacial tension. Furthermore, a slightly higher wall shear stress is observed along the refractory sample wall around the gas/slag interface, which could be attributed to the gas/slag interface fluctuation and Marangoni effect. As a result, the refractory around the gas/slag interface would be damaged by the molten slag, as shown in **Fig. 5**. The wear rate of the refractory sample in the vicinity of the gas/slag interface exceeds that elsewhere. The MgO within the refractory sample is thus constantly transferred into the molten slag, and then started to spread in the molten slag layer. **Fig. 6** represents the refractory sample morphology after the static testing. The sample shape change is negligibly small, and the corrosion traces induced by the molten slag could be clearly observed around the gas/slag interface. The difference from the simulated results is that the slag infiltration would slightly swell the refractory. Some new liquid phases were created after the infiltration in the experiment because of the interaction between the impurities and the molten slag. Moreover, some residual slag would adhere to the refractory. These are the reasons for the refractory swelling at the gas/slag interface. The above phenomena, however, was ignored in the simulation.

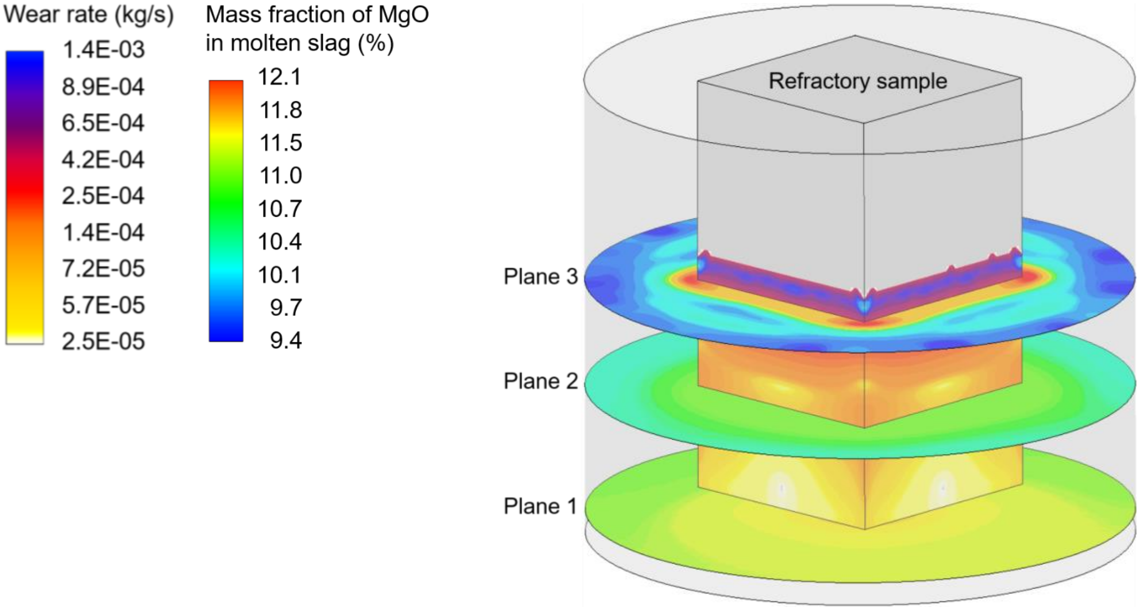

Fig. 5 – Corrosion rate distribution along the refractory sample wall and bottom, and MgO mass fraction distribution within the molten slag in the static experiment at 25 min.

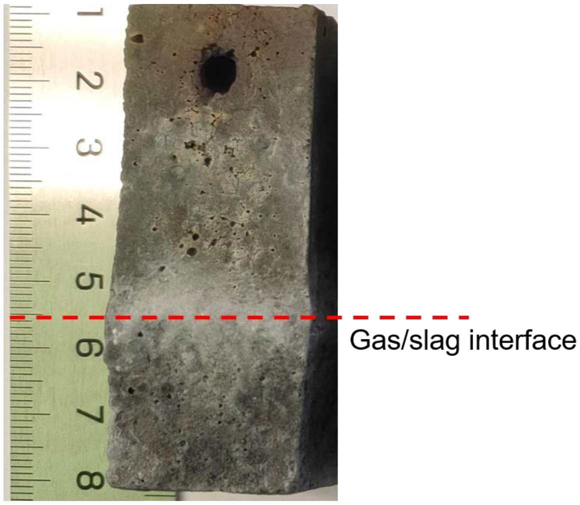

Fig. 6 – Refractory sample morphology after the static experiment.

B. *Morphology Evolution of Refractory Sample in Rotating Finger Testing*

As mentioned above, the refractory sample rotated in the molten slag with a constant 120 rpm rotation speed in the dynamic testing. **Fig. 7** displays the distribution of the wall shear stress along the refractory sample wall and bottom after 15 min. A higher wall shear stress is noted at the corner of the wall since it is a cuboid sample. Furthermore, the dissolution of the refractory occurs at the peripheral of the sample bottom, resulting in a shape change as indicated in **Fig. 7**. It is well known that refractory dissolution is generated due to the combined effect of flow-induced erosion and chemical-induced corrosion at this moment, where the former promotes the latter. In turn, the chemical-induced corrosion negatively affects the fluid flow because the dissolution of the refractory sample reduces its volume and stirring power to the molten slag. **Fig. 8** indicates the flow pattern in the molten slag with a 120 rpm stirring. The molten slag flows in the counterclockwise direction, and four small concomitant clockwise vortices are generated. **Fig. 9** exhibits the distribution of the overall wear rate. As expected, a greater wear rate is detected where a higher wall shear stress is observed. Compared with **Fig. 5**, the overall wear rate in the rotating finger testing is two orders of magnitude higher than that in the static testing, which implies the flow-induced erosion could significantly influence the refractory damage behavior.

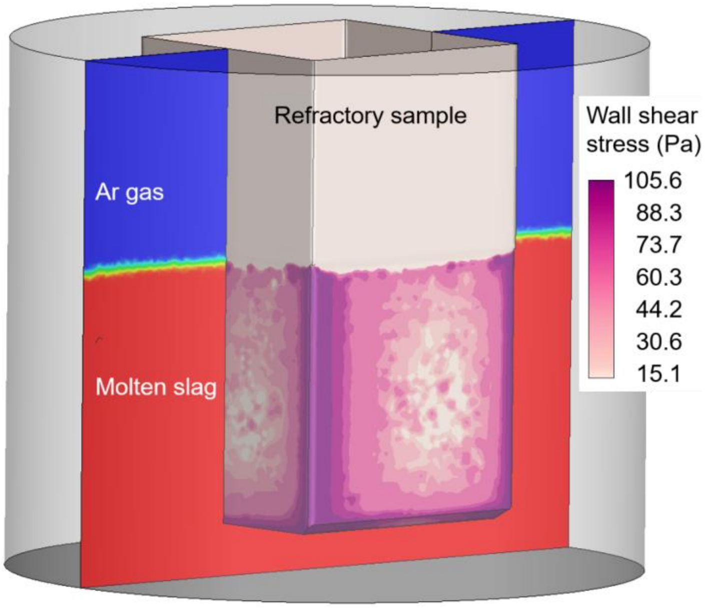

Fig. 7 – Wall shear stress distribution along the refractory sample wall and bottom in the dynamic experiment with a 120 rpm rotation speed at 15 min.

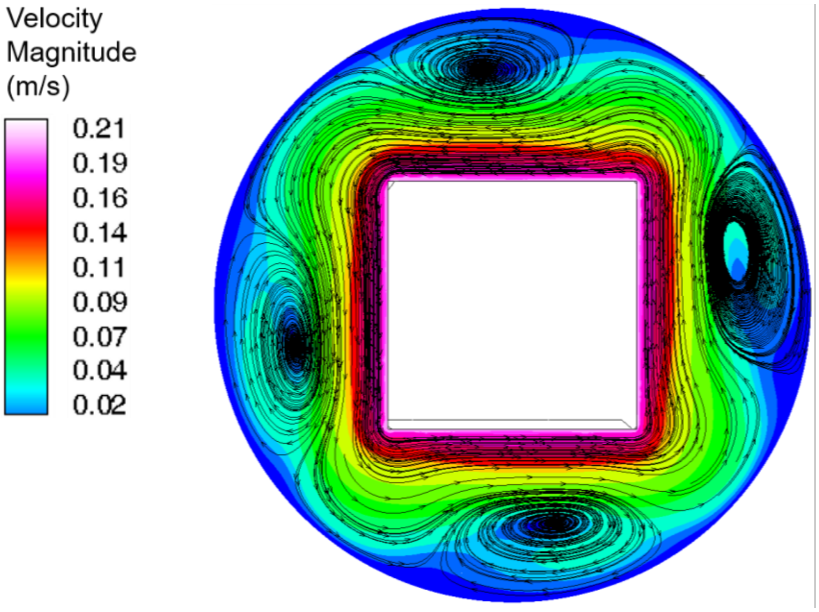

Fig. 8 – Distribution of flow pattern on plane 1 (the position of plane 1 is specified in Fig. 5) in the dynamic experiment with a 120 rpm rotation speed at 15 min.

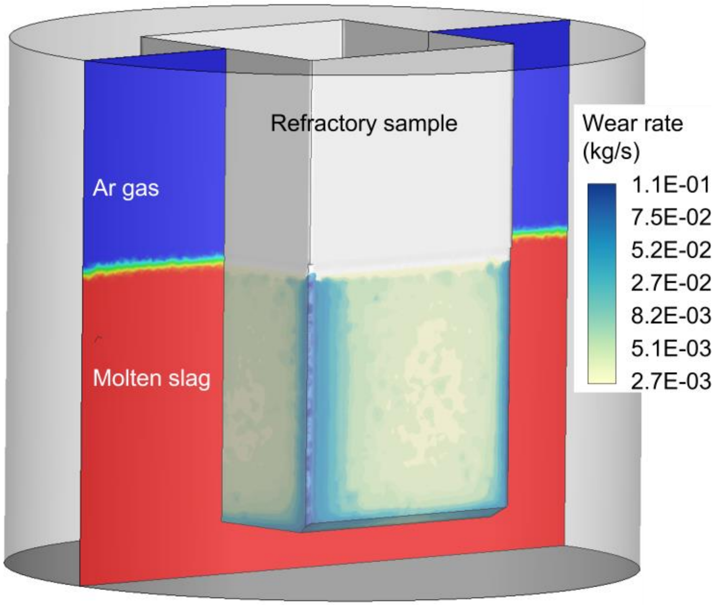

Fig. 9 – Wear rate distribution along the refractory sample wall and bottom in the dynamic experiment with a 120 rpm rotation speed at 15 min.

The MgO in the refractory sample would be continuously transferred into the molten slag because of the refractory dissolution, and then redistributed along with the flow, as demonstrated in **Fig. 10**. It can be seen that the distribution of the MgO content in the bulk of the molten slag is non-uniform, which could be attributed to the complicated flow pattern. However, the difference between the maximum (13.7 %) and the minimum (11.8 %) is relatively small because the volume of the reaction crucible, after all, is limited. **Fig. 11** represents the distribution of the MgO content along the refractory sample wall and bottom. MgO at the corner of the wall and bottom would first dissolve in the molten slag.

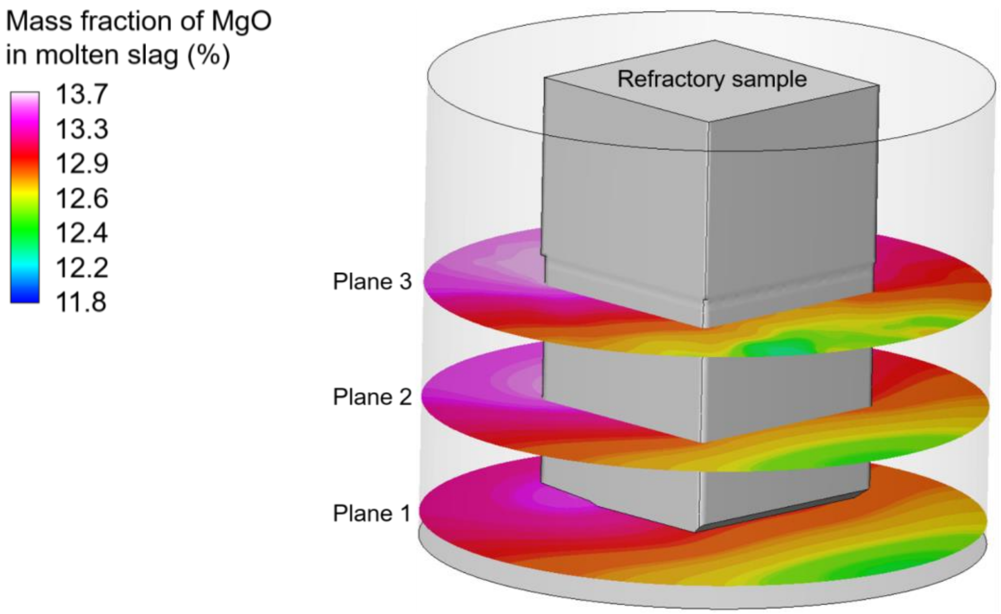

Fig. 10 – MgO mass fraction distribution within the molten slag in the dynamic experiment with a 120 rpm rotation speed at 15 min.

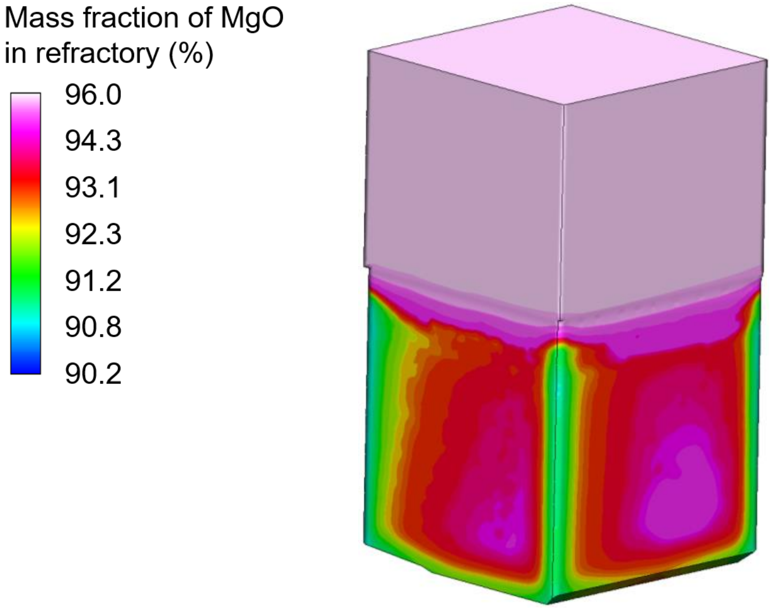

Fig. 11 – MgO mass fraction distribution along the refractory sample wall and bottom in the dynamic experiment with a 120 rpm rotation speed at 15 min.

The dissolution of the refractory sample becomes increasingly severe over time as shown in **Fig. 12**. The lower part of the refractory sample is gradually dissolved, because the lower part of the wall as well as the bottom provide a larger reaction area for the flow-induced erosion and chemical-induced corrosion. The dissolution of the lower part refractory sample is, therefore, more severe than that of the upper part. The MgO content distribution pattern also changes with refractory sample dissolution. At the early stage, the distribution of the MgO in the molten slag is relatively uniform because the molten slag could be mixed well with a sufficiently long sample. However, the MgO content at the lower part of the molten slag becomes lower than that at the upper part at the later period of the testing, as shown in **Fig. 12(c)**. On the one hand, no more MgO would be transferred into the molten slag from the refractory sample, since the lower part of the refractory sample has already been dissolved. On the other hand, the bottom molten slag would slow down because it could not be stirred anymore. **Fig. 13** denotes the flow pattern of the molten slag after 20 min. The maximum and average velocity magnitude are smaller than that after 15 min, as specified in **Fig. 8**. The small concomitant vortices also disappear.

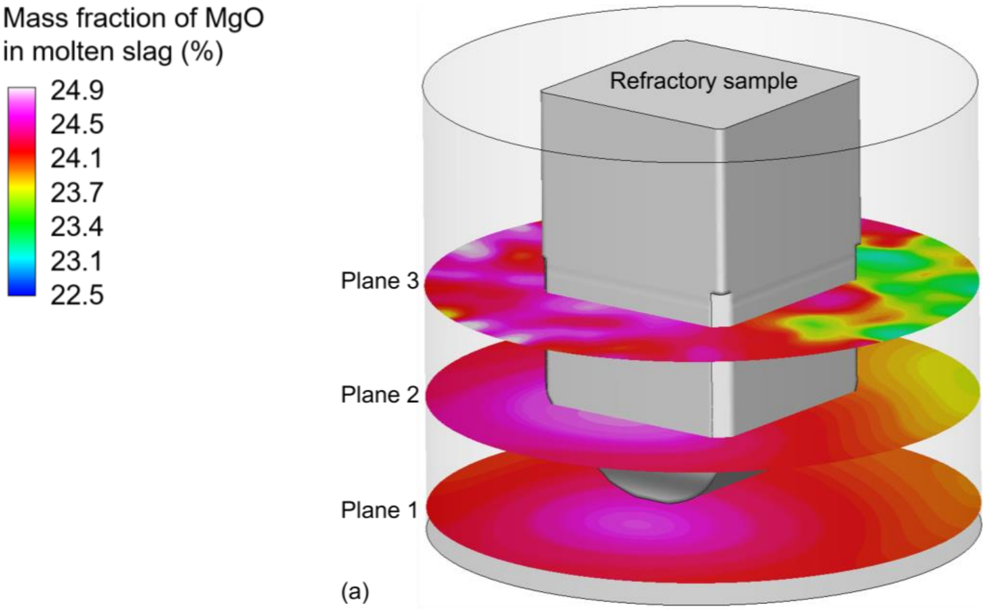

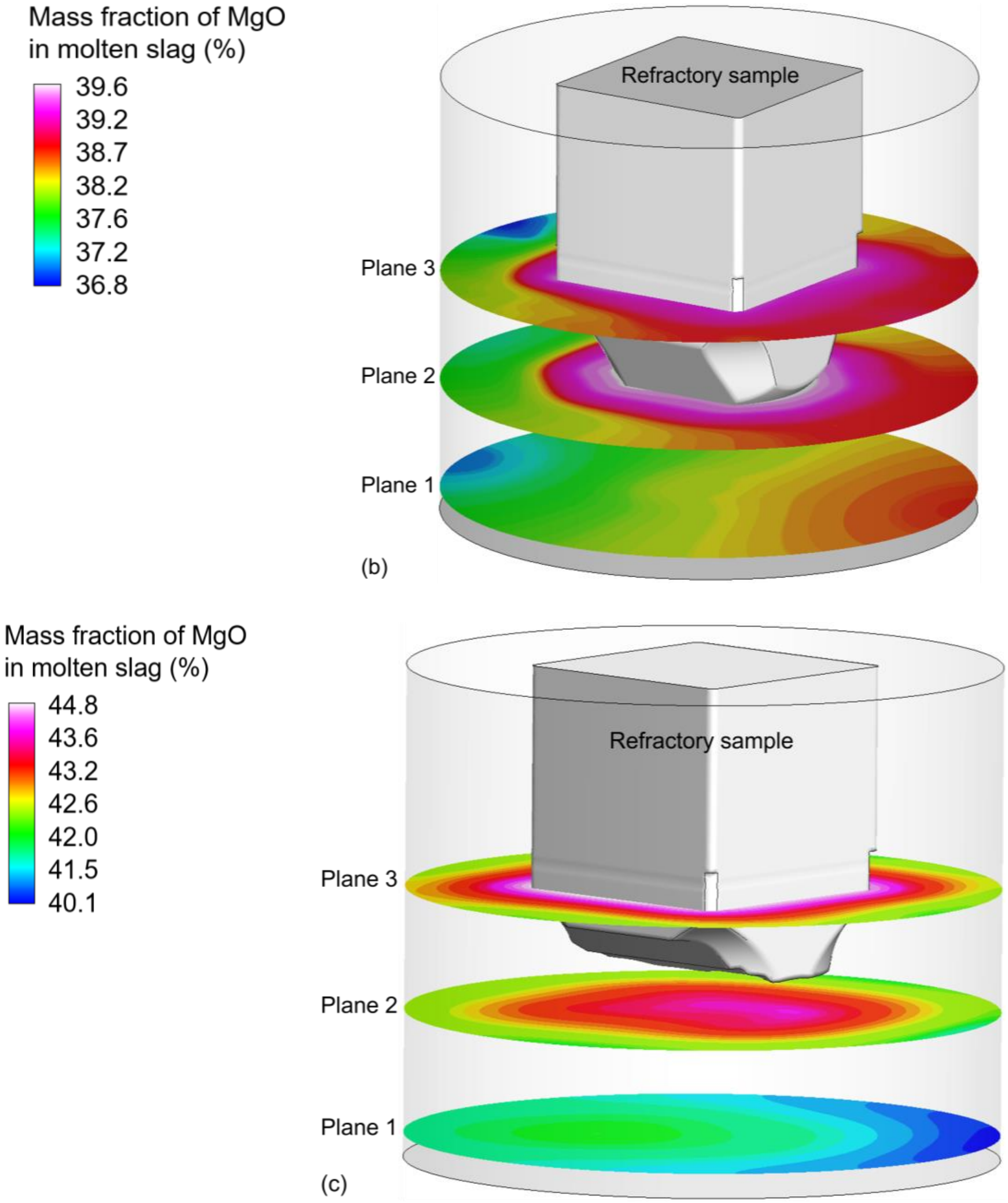

Fig. 12 – Refractory sample morphology and MgO mass fraction distribution along the refractory sample wall and bottom in the dynamic experiment with a 120 rpm rotation speed: (*a*) 17 min, (*b*) 20 min, and (*c*) 25 min.

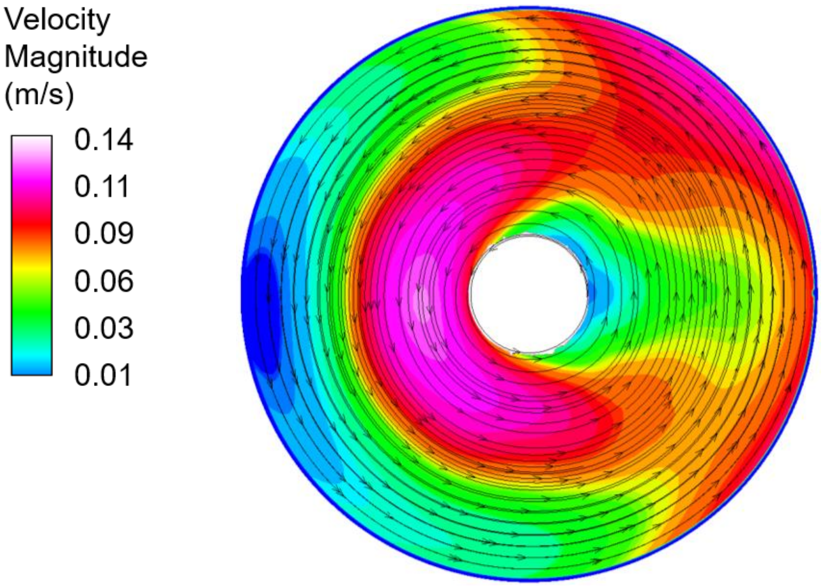

Fig. 13 – Distribution of flow pattern on plane 1 in the dynamic experiment with a 120 rpm rotation speed at 20 min.

At the end of the dynamic testing, only a small piece of the refractory sample remained in the molten slag as shown in **Fig. 14**. The wall shear stress along the refractory sample wall becomes smaller. Due to a smaller MgO content difference and inactive fluid flow, the wear rate of the refractory sample decreases accordingly, as demonstrated in **Fig. 15**.

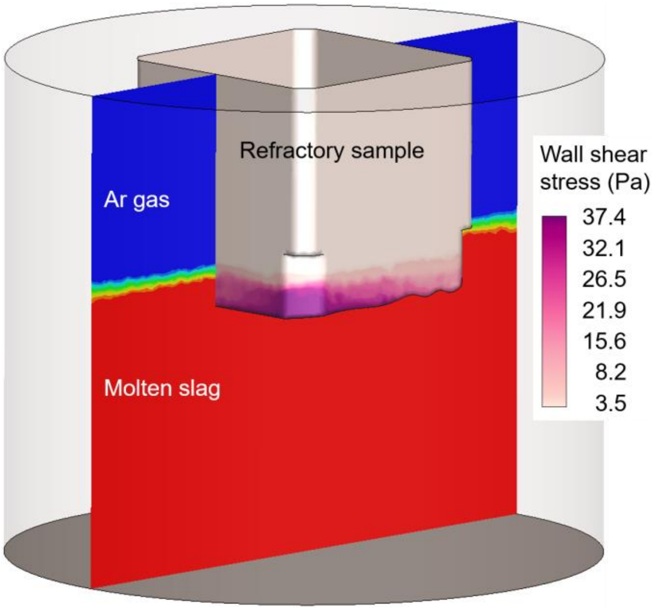

Fig. 14 – Wall shear stress distribution along the refractory sample wall and bottom in the dynamic experiment with a 120 rpm rotation speed at 30 min.

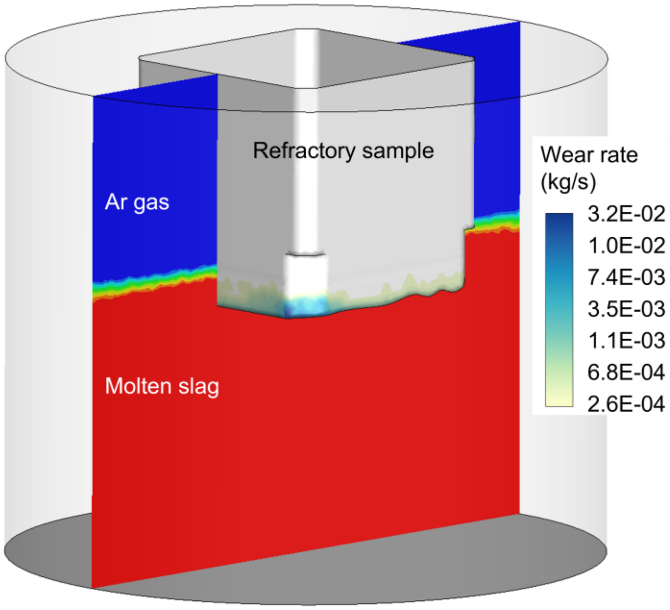

Fig. 15 – Wear rate distribution along the refractory sample wall and bottom in the dynamic experiment with a 120 rpm rotation speed at 30 min.

C. *Model Validation*

The present work aims to develop a reliable numerical model to predict refractory damage behavior. It is therefore necessary to thoroughly compare the experimental and numerical results. **Fig. 16** represents the evolution of the MgO mass fraction with time at the monitoring point in the static and rotating finger testings. A reasonable agreement is obtained between the measurement and simulation results. However, the measured MgO mass fractions always exceeded the simulated data in the static testing because the slag corrosion and the refractory matrix dissolution after the slag infiltration, which could promote the refractory damage, were not modeled in the numerical simulation. Besides, the MgO mass fraction rapidly increases after 15 min of the rotating finger testing. The wear rate of the refractory sample exceeds the threshold value, giving rise to the damage of the refractory sample, under the continuous action of flow-induced erosion and chemical-induced corrosion. The MgO content thus speedily increases due to the refractory sample dissolution.

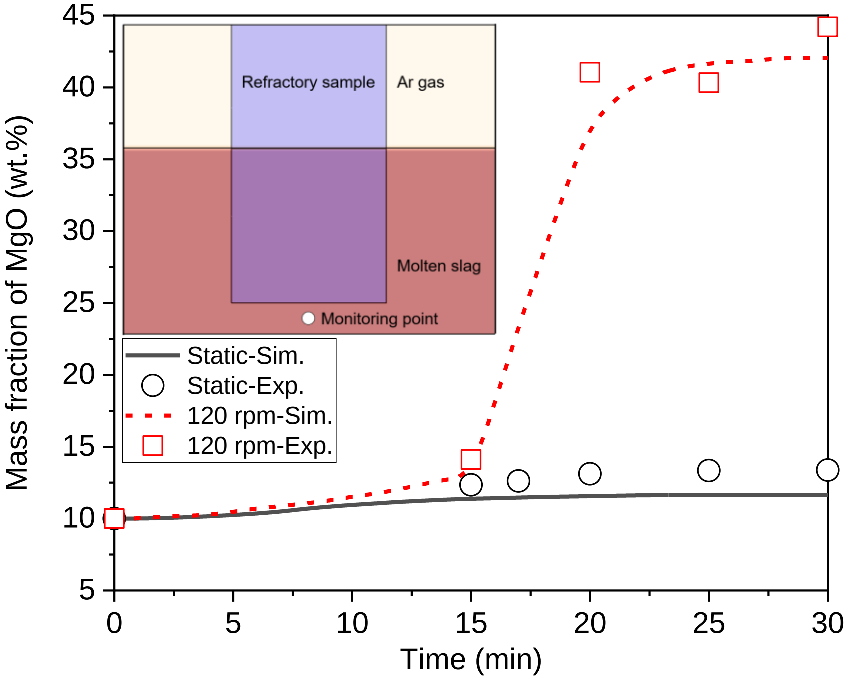

Fig. 16 – Evolution of MgO mass fraction with time at the monitoring point.

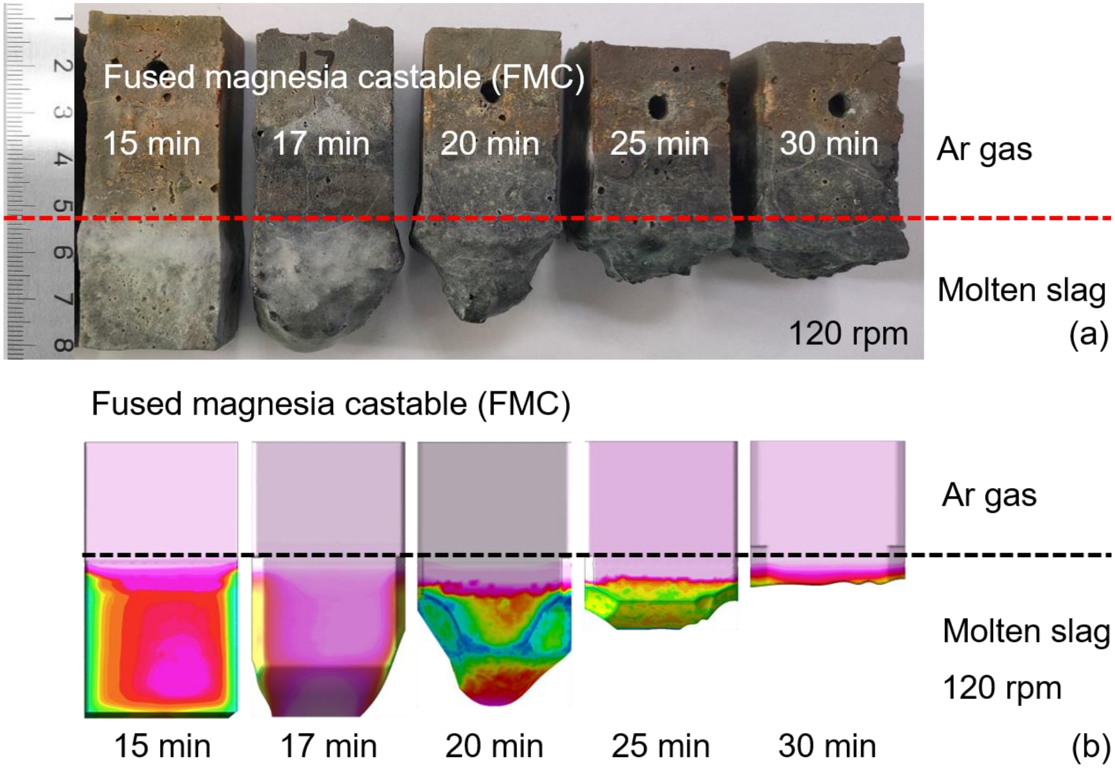

Fig. 17 – Comparison of the refractory sample morphology between the (*a*) experiment and (*b*) simulation.

Fig. 17 compares the refractory sample morphology between the experiment and simulation. The observed and calculated sample morphologies are similar. It is clear that the cuboid bottom refractory sample gradually shifts to the cone and finally becomes flat with the progress of refractory dissolution.

Fig. 18 compares the refractory mass loss rate of the refractory sample between the experiment and simulation. The established numerical model could give relatively accurate prediction of the varying refractory sample mass loss with time. Moreover, the measured mass loss rates always exceeds than the calculated data because the slag corrosion and the refractory matrix dissolution after the slag infiltration are not considered in the numerical model, which underestimates the mass loss rate accordingly.

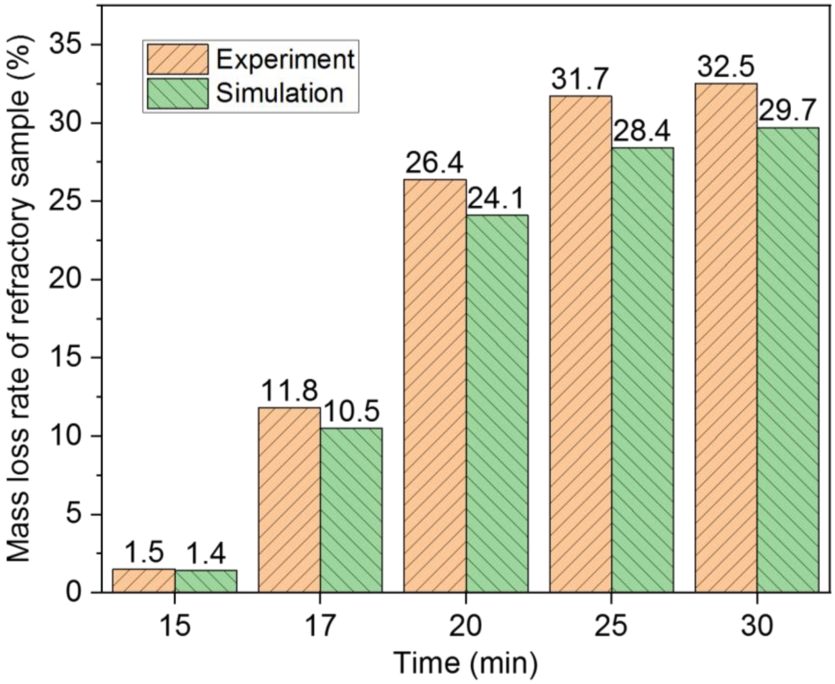

Fig. 18 – Comparison of the refractory sample mass loss rate between the experiment and simulation.

In general, the developed numerical model in the present work could describe the refractory damage behavior with acceptable accuracy. The agreement between the model results and the experimental data gives confidence in the fundamental validity of the developed numerical model. Besides assessing of the predicate capability of the developed numerical model to identify the magnesia lining damage behaviors of various metallurgical vessels, the numerical model may also support the planning of inspections and decisions on smelting plant operation. In most cases, only qualitative or empirical data are available on the effects of these process variables on the refractory lining damage. For effective refining of molten steel, quantitative information should be provided, such as slag component variation, lining wear rate, and lining shape change. Therefore, the present work has developed and validated a comprehensive numerical model predicting the fluid flow, heat transfer, and refractory lining erosion and corrosion behaviors.

It could be noted that some assumptions in the present model are far away from actual situation. The undissolved solid refractory fragments in the molten slag were ignored. In the experiment, these fragments tended to sink to the bottom because of a higher density. The delaminated refractory fragments however were supposed to dissolve in the molten slag in the liquid state in the numerical model for simplification. To quantitatively describe the refractory shape change, the fluid-solid coupled algorithm and dynamic mesh method were adopted. The reduced volume of the solid region was filled with the same volume of liquid for avoiding mass non-conservation during the numerical solution procedure. Besides, the influence of the MgO saturation concentration on the chemical corrosion was not included. The chemical corrosion would become weaker when the MgO content gradually approaches its saturation content, and completely stop if the MgO dissolution reaches saturation condition. Actually, the limitation of the saturation concentration could create a great effect on the refractory wear behavior. The effect of these two factors will be numerically investigated in our next work.

VI. CONCLUSIONS

To quantitatively estimate the magnesia refractory deterioration in the smelting process, static and rotating finger experiments were carried out to assess the magnesia refractory dissolution. Next, a transient 3D fluid-solid coupled numerical model was developed, which involved the gas/slag two-phase flow pattern, temperature profile, MgO content distribution, solid refractory dissolution, and sample shape change. Furthermore, a degradation kinetic model was proposed to calculate the refractory wear rate determined by the coupled effect of the flow-induced erosion and chemical-induced corrosion. In addition to the wall shear stress, temperature, and MgO content difference, it also considered the molten slag’s wetting behavior. The shape change of the solid refractory sample was represented by the dynamic mesh. A reasonable agreement between the predicted results and measured data proved the feasibility of the developed numerical model. The main findings can be summarized as follows:

(1) The molten slag first infiltrates the porous refractory, eroding and dissolving the matrix, and peels the aggregate under the flow action. The simulated wear rate is underestimated compared with the measured data, because the slag corrosion and the matrix dissolution are neglected in the numerical model.

(2) Flow-induced erosion must be considered in estimating the refractory wear rate. The wear rate would be increased by one or two orders of magnitude by the flow action, depending on the velocity.

(3) The powers of the wall shear stress are successfully used to evaluate flow-induced erosion behavior. At the same time, a modified Arrhenius’s law related to the composition content difference, temperature, and corrosion activation energy is adopted to assess the chemical-induced corrosion.

ACKNOWLEDGEMENTS

The authors appreciate the financial support of this study from the Young Elite Scientist Sponsorship Program by the China Association for Science and Technology (Grant No. YESS20200210) and the National Natural Science Foundation of China (Grant Nos. U1860205 and U21A2058).

CONFLICT OF INTEREST

The authors declare that they have no conflicts of interest to disclose.

REFERENCES

1. G.Y. Wu, W. Yan, S. Schafföner, Y.J. Dai, B.Q. Han, T.Q. Li, S.B. Ma, N. Li, and G.Q. Li: *J. Alloys Compd.*, 2019, vol. 796, pp. 131-7.
2. Y.J. Dai, Y.W. Li, X.F. Xu, Q.Y. Zhu, W. Yan, S.L. Jin, and H. Harmuth: *J. Eur. Ceram. Soc.*, 2019, vol. 39(16), pp. 5433-41.
3. F.Q. Gu, Y.B. Zhang, Y.K. Tu, X.T. Wu, Y.X. Zhu, Y.Y. Long, and D.S. Shen: *Ceram. Int.*, 2022, vol. 48(9), pp. 13100-7.
4. M. Kalantar, B.M. Moshtaghioun, and A. Monshi: *J. of Materi. Eng. Perform.*, 2010, vol. 19, pp. 237-245.
5. Q. Zhao, X. Zheng, C.J. Liu, M.F. Jiang, H. Saxén, and R. Zevenhoven: *Steel Res. Int.*, 2021, vol. 92(4), 2000497.
6. D.H. Kim, S.H. Yoo, C.S. Ha, J.M. Park, K.S. Lee, and S.M. Kim: *J. Ceram. Soc. Jpn.*, 2005, vol. 113(1318), pp. 405-8.
7. S. Samadi, S.L. Jin, D. Gruber, and H. Harmuth: *Int. J. Mech. Sci.*, 2021, vol. 197, 106345.
8. Y. Murakami, Y. Matsuzaki, T. Kamimura, T. Nishiura, K. Masuda, A. Shibayama, and R. Inoue: *Ceram. Int.*, 2020, vol. 46(7), pp. 9281-8.
9. C.Y. Liu, X. Gao, S. Ueda, M.X. Guo, and S.Y. Kitamura: *ISIJ Int.*, 2020, vol. 60(9), pp. 1835-48.
10. J.J. Wang, L.F. Zhang, G. Cheng, Q. Ren, and Y. Ren: *Int. J. Miner. Metall. Mater.*, 2021, vol. 28, pp. 1298-308.
11. C. Yuan, Y. Liu, G.Q. Li, Y.S. Zou, and A. Huang: *Ceram. Int.*, 2022, vol. 48(1), pp. 427-35.
12. J.H. Park and L.F. Zhang: *Metall. Mater. Trans. B,* 2020, vol. 51B(6), pp. 2453-82.
13. Y.Z. Huo, H.Z. Gu, J. Yang, A. Huang, and Z. Ma: *J. Iron Steel Res. Int.*, 2022, vol. 29, pp. 1110-8.
14. P.H.R. Vaz de Melo, J.J.M. Peixoto, G.S. Galante, B.H.M. Loiola, C.A. da Silva, I.A. da Silva, and V. Seshadri: *J. Mater. Res. Tech.*, 2019, vol. 8(5), pp. 3764-71.
15. Q. Wang, C. Liu, L.P. Pan, Z. He, G.Q. Li, and Q. Wang: *Metall. Mater. Trans. B*, 2022, vol.

53B(3), pp. 1617-30.

16. Q. Wang, C. Tan, A. Huang, W. Yan, H.Z. Gu, Z. He, and G.Q. Li: *Metall. Mater. Trans. B*, 2021, vol. 52B(5), pp. 3265-75.
17. Q. Wang, C. Tan, A. Huang, W. Yan, H.Z. Gu, Z. He, and G.Q. Li: *Metall. Mater. Trans. B*, 2021, vol. 52B(3), pp. 1344-56.
18. C. Liu, A.D. Xiao, Z. He, W. Yan, G.Q. Li, and Q. Wang: *Steel Res. Int.*, 2022, DOI: https://doi.org/10.1002/srin.202100818.
19. L.Q. Wang, H.Y. Zhu, J.X. Zhao, M.M. Song, and Z.L. Xue: *Ceram. Int.*, 2022, vol. 48(1), pp. 1090-7.
20. C.W. Andrés, M.N. Moliné, S. Camelli, and A.G.T. Martinez: *Ceram. Int.*, 2020, vol. 46(15), pp. 24495-503.
21. J. Poirier, E. Blond, E. de Bilbao, R. Michel, A. Coulon, J. Gillibert, M. Boussuge, Y. Zhang, D. Ryckelynk, G. Dusserre, T. Cutard, and P. Leplay: *Metall. Res. Tchnol.*, 2017, vol. 114(6), 610.
22. D.L. You, S.K. Michelic, and C. Bernhard: *Steel Res. Int.*, 2020, vol. 91(11), 2000045.
23. J. Lee, J. Myung, and Y.S. Chung: *Metall. Mater. Trans. B*, 2021, vol.52B(3), pp. 1179-85.
24. J. Guarco, H. Harmuth, and S. Vollmann: *Int. J. Heat Mass Transf.*, 2022, vol. 186, 122494.
25. F. Huang, C. Liu, N. Maruoka, and S.Y. Kitamura: *Ironmak. Steelmak.*, 2015, vol. 42(7), pp. 553-60.
26. H.J. Wang, R. Caballero, and S.C. Du: *J. Eur. Ceram. Soc.*, 2018, vol. 38(2), pp. 789-97.
27. S. Jansson, V. Brabie, and P. Jönsson: *Scand. J. Metall.*, 2005, vol. 34(5), pp. 283-92.
28. J. Liu, M. Guo, P.T. Jones, F. Verhaeghe, B. Blanpain, and P. Wollants: *J. Eur. Ceram. Soc.*, 2007, vol. 27(4), pp. 1961-72.
29. S. Zhang and W.E. Lee: *J. Eur. Ceram. Soc.*, 2001, vol. 21(13), pp. 2393-405.
30. L.P. Fu, H.Z. Gu, A. Huang, S.W. Or, Y. Zou, Y.S. Zou, and M.J. Zhang: *J. Eur. Ceram. Soc.*, 2022, vol. 42(3), pp. 744-763.
31. Y. Kim, Y. Kashiwaya, and Y.S. Chung: *Ceram. Int.*, 2020, vol. 46(5), pp. 6205-11.

32. S. Amini, M. Brungs, S. Jahanshahi, and O. Ostrovski: *ISIJ Int.*, 2006, vol. 46(11), pp. 1554-9.
33. Y. Zou, H.Z. Gu, A. Huang, and M.J. Zhang: *Ceram. Int.*, 2014, vol. 40(5), pp. 7023-8.
34. A. Huang, H.Z. Gu, Y.S. Zou, L.P. Fu, P.F. Lian, and L.W. Jin: *Ceram. Trans. Ser.*, 2016, vol. 256, pp. 101-11.
35. C.W. Hirt and B.D. Nichols: *J. Comput. Phys.*, 1981, vol. 39(1), pp. 201-25.
36. J.U. Brackbill, D.B. Kothe, and C. Zemach: *J. Comput. Phys.*, 1992, vol. 100(2), pp. 335-54.
37. E. Heinl and M. Bohnet: *Powder Technol.*, 2005, vol. 159(2), pp. 95-104.
38. Y. He, A.E. Bayly, and A. Hassanpour: *Powder Technol.*, 2018, vol. 325, pp. 620-31.
39. C. Paz, E. Suárez, M. Conda, and J. Vence: *Heat Transf. Eng.*, 2020, vol. 41(2), pp. 199-207.
40. X. Yang, H. Zhou and H. Wu: *Fuel*, 2022, vol. 316, 123250.
41. C.F. Du and M.L. Bian: *Case Stud. Therm. Eng.*, 2018, vol. 12, pp. 117-25.
42. E. Karimi-Sibaki, A. Kharicha, J. Bohacek, M. Wu, and A. Ludwig: *Metall. Mater. Trans. B*, 2015, vol. 46B(5), pp. 2049-61.
43. J.L. Svantesson, B. Glaser, M. Ersson, J.F. White, M. Imris, and P.G. Jönsson: *Ironmak. Steelmak.*, 2021, vol. 48(5), pp. 607-18.
44. C. Sagadin, S. Luidold, C. Wagner, C. Pichler, D. Kreuzer, A. Spanring, H. Antrekowitsch, A. Clarke, and K. Clarke: *Metall. Mater. Trans. B*, 2021, vol.52B(2), pp. 1052-60.
45. D. Kumar, K.C. Ahlborg, and P.C. Pistorius: *Metall. Mater. Trans. B*, 2019, vol. 50B(5), pp. 2163-74.
46. L.P. Fu, H.Z. Gu, and A. Huang: *J. Am. Ceram. Soc.*, 2015, vol. 98(5), pp. 1658-63.
47. J. Rieger, M. Drózd-Ryś, C. Weiss, and H. Harmuth: *Steel Res. Int.*, 2014, vol. 85(4), pp. 527-36.
48. A.P. Luz, F.C. Leite, M.A.M. Brito, and V.C. Pandolfelli: *Ceram. Int.*, 2013, vol. 39(7), pp. 7507-15.
49. S. Vollmann and H. Harmuth: *Adv. in Sci. Technol.*, 2010, vol. 70, pp. 199-204.
50. T. Kargul and J. Falkus: *Steel Res. Int.*, 2010, vol. 81(11), pp. 953-8.

51. Q. Wang, F.G. Tan, Z. He, G.Q. Li, and J.L. Li: *JOM*, 2021, vol. 73(9), pp. 2709-14.

52. M. Liu and P. Mostaghimi: *Int. J. Heat Mass Transf.*, 2018, vol. 120, pp. 194-201.

53. M. Liu and P. Mostaghimi: *Chem. Eng. Sci.*, 2018, vol. 190, pp. 436-42.

54. A. Menendez Blanco and J.M. Fernandez Oro: *Comput. Fluids*, 2012, vol. 57, pp. 138-50.

55. ANSYS Fluent User’s Guide, Release 2020R1, ANSYS Inc., 2020.

56. Y.S. Zou, A. Huang, R.F. Wang, L.P. Fu, H.Z. Gu, and G.Q. Li: *Corros. Sci.*, 2020, vol. 167, 108517.

57. **Table Captions:**

Table I. Preparation formula of the refractory sample (wt. %)

Table II. Initial composition of molten slag (wt.%)

Table III. Physical Properties and Operating Conditions

Figure Captions:

Fig. 1 – Experimental setup.

Fig. 2 – Physical model of the computational domain.

Fig. 3 – Distributions of the temperature and the gas-slag two phases in the static experiment at 25 min.

Fig. 4 – Wall shear stress distribution along the refractory sample wall and bottom in the static experiment at 25 min.

Fig. 5 – Corrosion rate distribution along the refractory sample wall and bottom, and MgO mass fraction distribution within the molten slag in the static experiment at 25 min.

Fig. 6 – Refractory sample morphology after the static experiment.

Fig. 7 – Wall shear stress distribution along the refractory sample wall and bottom in the dynamic experiment with a 120 rpm rotation speed at 15 min.

Fig. 8 – Distribution of flow pattern on plane 1 (the position of plane 1 is specified in Fig. 5) in the dynamic experiment with a 120 rpm rotation speed at 15 min.

Fig. 9 – Wear rate distribution along the refractory sample wall and bottom in the dynamic experiment with a 120 rpm rotation speed at 15 min.

Fig. 10 – MgO mass fraction distribution within the molten slag in the dynamic experiment with a 120 rpm rotation speed at 15 min.

Fig. 11 – MgO mass fraction distribution along the refractory sample wall and bottom in the dynamic experiment with a 120 rpm rotation speed at 15 min.

Fig. 12 – Refractory sample morphology and MgO mass fraction distribution along the refractory sample wall and bottom in the dynamic experiment with a 120 rpm rotation speed: (*a*) 17

min, (*b*) 20 min, and (*c*) 25 min.

Fig. 13 – Distribution of flow pattern on plane 1 in the dynamic experiment with a 120 rpm rotation speed at 20 min.

Fig. 14 – Wall shear stress distribution along the refractory sample wall and bottom in the dynamic experiment with a 120 rpm rotation speed at 30 min.

Fig. 15 – Wear rate distribution along the refractory sample wall and bottom in the dynamic experiment with a 120 rpm rotation speed at 30 min.

Fig. 16 – Evolution of MgO mass fraction with time at the monitoring point.

Fig. 17 – Comparison of the refractory sample morphology between the (*a*) experiment and (*b*) simulation.

Fig. 18 – Comparison of the refractory sample mass loss rate between the experiment and simulation.